Surface diffusivity of cleaved NaCl crystals as a function of humidity: Impedance spectroscopy measurements and implications for crack healing in rock salt

Paula J. Koelemeijer,[1,2] Colin J. Peach,[1] and Christopher J. Spiers[1]

Received 26 June 2011; revised 20 November 2011; accepted 22 November 2011; published 21 January 2012.

[1] Rock salt offers an attractive host rock for geological storage applications, because of its naturally low permeability and the ability of excavation-induced cracks to heal by fluid-assisted diffusive mass transfer. However, while diffusive transport rates in bulk NaCl solution are rapid and well characterized, such data are not directly applicable to storage conditions where crack walls are coated with thin adsorbed water films. To reliably predict healing times in geological storage applications, data on mass transport rates in adsorbed films are needed. We determined the surface diffusivity in such films for conditions with absolute humidities (AH) ranging from 1 to 18 g/m^3 (relative humidities (RH) of 4%–78%) by measuring the surface impedance of single NaCl crystals. We use the impedance results to calculate the effective surface diffusivity $S = D\delta C$ using the Nernst-Einstein equation. The S values obtained lie in the range 1×10^{-27} m^3 s^{-1} at very dry conditions to 1×10^{-19} m^3 s^{-1} for the deliquescence point at 296 K, which is in reasonable agreement with existing values for grain boundary diffusion under wet conditions. Estimates for the diffusivity D made assuming a film thickness δ of 50–90 nm and no major effects of thickness on the solubility C lie in the range of 1×10^{-14} to 8×10^{-12} m^2 s^{-1} for the highest humidities studied (14–18 g/m^3 AH, 60%–78% RH). For geological storage systems in rock salt, we predict S values between $1 \times 10^{-22} - 8 \times 10^{-18}$ m^3 s^{-1}. These imply crack healing rates 6 to 7 orders of magnitude lower than expected for brine-filled cracks.

Citation: Koelemeijer, P. J., C. J. Peach, and C. J. Spiers (2012), Surface diffusivity of cleaved NaCl crystals as a function of humidity: Impedance spectroscopy measurements and implications for crack healing in rock salt, *J. Geophys. Res.*, *117*, B01205, doi:10.1029/2011JB008627.

1. Introduction

[2] Rock salt has long been recognized as a highly suitable medium for geological storage of oil, gas and hazardous wastes because of its low-permeability, high-ductility, low-creep strength and capacity for self-healing by plastic flow and diffusive mass transfer [*Langer*, 1993; *Cosenza and Ghoreychi*, 1999; *Ewing*, 1999; *Langer*, 1999; *Silberschmidt and Silberschmidt*, 2000; *Liang et al.* 2007]. At present, the growing needs to reduce CO_2 emissions and to improve energy security are leading to renewed interest in rock salt as a geological storage medium. Solution-mined caverns are being reconsidered for commercial and strategic storage of oil, (liquid) natural gas and hydrogen fuel. They are also being considered for storage of energy in the form of compressed air, as a means of buffering wind, solar and tidal energy supplies [*Hou et al.*, 2010]. Conventional mines and deep boreholes in rock salt are still on the agenda as possible sites for disposal of radioactive waste. In addition, rock salt overlying depleted oil and gas reservoirs offers a highly favorable caprock for geological storage of CO_2 in such reservoirs, provided that boreholes through the salt can be effectively sealed.

[3] In all of the above cases, the sealing capacity of the storage system is determined by competition between (1) dilatant (micro)crack damage induced in the salt by its convergence creep response to excavation or drilling, and (2) the closure, healing and sealing of (micro)cracks. Much work has been done on mechanical behavior, dilatancy and creep-induced damage in rock salt [*Senseny et al.*, 1992; *Hunsche and Hampel*, 1999; *Silberschmidt and Silberschmidt*, 2000; *Alkan et al.*, 2007; *Liang et al.*, 2007]. This has led to a range of shear stress versus mean stress criteria for damage and permeability development in salt, allowing mapping of the dilatant damage zone, or excavation disturbed zone (EDZ), expected to develop around cavities due to purely mechanical effects [*Cristescu and Hunsche*, 1998]. However, much less is known about the healing of (micro)crack damage in such zones and how this affects the extent and transport properties of the EDZ. This is of key importance for assessing the long-term barrier function of salt, since it is not known how long (micro)cracks in the EDZ may remain open, notably around

[1]High Pressure and Temperature Laboratory, Faculty of Geosciences, Utrecht University, Utrecht, Netherlands.
[2]Now at Bullard Laboratories, Department of Earth Sciences, University of Cambridge, Cambridge, UK.

0148-0227/12/2011JB008627

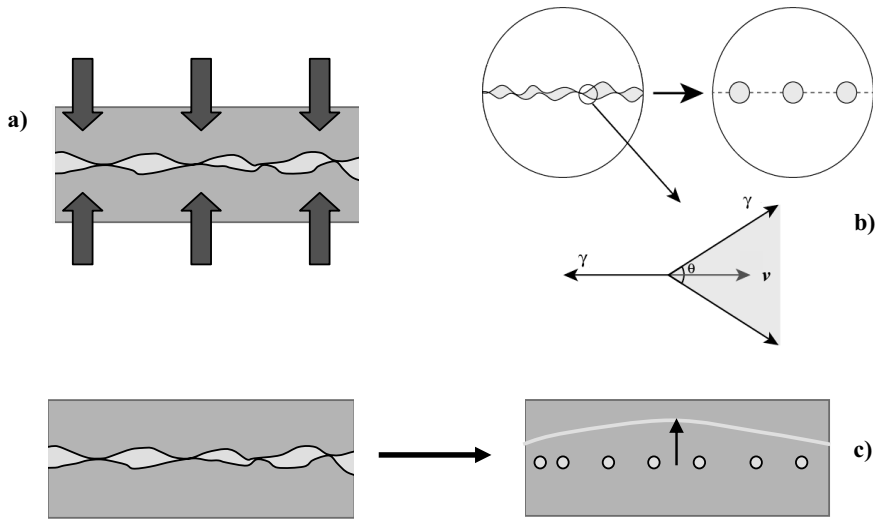

Figure 1. Physical mechanisms by which crack healing/sealing and permeability reduction can occur in the EDZ. (a) Mechanical closure of cracks in association with compaction of the bulk rock by elastic deformation or plastic flow. (b) Necking down of cracks and pores to form arrays of disconnected tubular and spherical inclusions, by means of surface energy driven mass transport facilitated by adsorbed water films or free pore brine. γ denotes the surface energy vectors, θ the dihedral angle of the crack and v the crack migration velocity. Wide cracks can also contract in length by this type of process, rather than or as well necking down into arrays of inclusions (Figure 2). (c) Crack and pore occlusion through fluid-assisted grain boundary migration (recrystallization).

openings in waste repositories or around boreholes in salt caprocks overlying CO_2 storage reservoirs.

1.1. Crack Healing Mechanisms

[4] In the EDZ, crack healing/sealing and permeability reduction can occur by three different physical mechanisms (Figure 1). First, in a regime of increasing mean normal stress, cracks can close mechanically due to compaction of the bulk rock by elastic deformation or crystal plasticity [e.g., *Chen et al.*, 1996; *Gavrilenko and Gueguen*, 1989; *Kim and Lee*, 2001]. The second mechanism is crack healing driven by surface energy reduction. This involves contraction and/or necking down of cracks, forming tubes and eventually isolated fluid inclusions [*Smith and Evans*, 1984; *Hickman and Evans*, 1987; *Brantley et al.*, 1990; *Spiers and Schutjens*, 1999; *Cinar et al.*, 2006]. Transport of material occurs by diffusion through thin water films adsorbed to the solid surface or filling the cracks completely. In this diffusive healing mechanism, material is dissolved and transported through a layer of brine to the area where precipitation occurs. The third mechanism, crack healing by recrystallization, is a process where grain boundary migration [*Peach et al.*, 2001; *ter Heege et al.*, 2004, 2005] overgrows a fluid-filled crack, leaving isolated, spherical fluid inclusions behind.

[5] Mechanical closure effects are expected to dominate damage and permeability reduction in the early stages of convergence of backfilled or plugged cavities, as this is when convergence rates are fastest and therefore when normal stresses build up most rapidly [*Liedtke and Bleich*, 1985; *Paraschiv-Munteanu and Cristescu*, 2001]. Mass transfer effects may be very rapid if cracks are filled with brine, since this allows rapid dissolution, diffusion and precipitation. However, if cracks are open and the walls only coated with adsorbed water, healing by grain boundary migration will be inhibited [*Peach et al.*, 2001] and healing by surface energy driven diffusion through the thin adsorbed water film might be very slow, warranting further consideration.

1.2. Effective Surface Diffusivity

[6] Microphysical models for diffusive crack healing and other diffusion controlled mass transfer processes occurring in fluid-saturated rock materials, such as intergranular pressure solution [e.g., *Rutter*, 1983; *Spiers et al.*, 1990; *ter Heege et al.*, 2004] or neck growth at grain contacts [e.g., *Hickman and Evans*, 1992; *Spiers and Schutjens*, 1999], all incorporate a kinetic term that expresses the diffusive properties of the fluid through which transport occurs. This diffusion product (the effective surface diffusivity) is generally written as $S = D\delta C$, where D is the diffusion coefficient of the dissolved solid, C the solubility of the solid in the adsorbed film and δ is the (mean) thickness of the fluid body through which diffusion occurs.

[7] For diffusive healing of a fluid filled, wedge-shaped crack (Figure 2), or for growth of the neck at a bicrystal contact, the tight, negative radius of curvature (r) at the crack tip or neck region leads to a decrease in chemical potential of the solid at these sites by an amount equal to $\gamma V_m/r$ relative to the potential at the crack wall or at grain wall sites [*Heidug*, 1991]. This leads to transport of mass from these sites to the crack tip or neck region, via a serial process of dissolution at the free wall sites, diffusion through the fluid phase and precipitation at the crack tip or neck sites. Since neck growth and crack tip migration by this process are geometrically equivalent in two-dimensions, we will refer to this process henceforth entirely in terms of crack growth.

[8] On the basis of several authors' work [*Smith and Evans*, 1984; *Heidug*, 1991; *Hickman and Evans*, 1987; *Hickman and Evans*, 1992; *Spiers and Schutjens*, 1999], it is

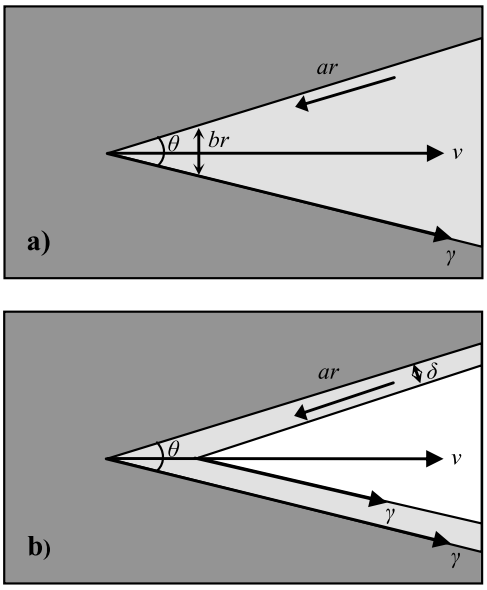

Figure 2. Geometric aspects of the single crack healing model. (a) Schematic drawing of a brine-filled crack. (b) Schematic drawing of a crack whose surface is coated by a thin water film. Healing and hence crack tip migration velocity v is driven by the surface curvature difference between the crack tip or cusp and the flat crack walls. The parameters indicated appear in equation (1) and are defined in Table 1.

easily shown that the velocity v (m/s) of crack tip (or neck) migration is given by

$$v = \frac{DCV_m\gamma}{\pi RT}\frac{\lambda}{a}\frac{\cos(\theta/2)}{r^2}, \quad (1)$$

where in case of brine-filled cracks γ is the solid–liquid interfacial energy, θ is the opening angle of the crack, V_m is the molar volume of the solid phase, a/b is the ratio of the mean transport distance ar to the mean cross section for diffusion br, and $\lambda = b/2$. All symbols and parameter values used in this paper are listed in Table 1. In the case where crack walls are coated by a thin adsorbed aqueous film, γ is approximated by the sum of the solid–liquid and vapor–liquid interfacial energy and λ is given by δ/r where δ is the thickness of the film.

[9] For brine-filled cracks, the thickness and hence cross section br of fluid available for diffusion will be much greater than the thickness δ available for diffusion in a thin adsorbed film. Moreover, D and C may take different values in an adsorbed aqueous film than in bulk solution, with D being potentially much lower in the film case [*Rutter*, 1983; *de Meer et al.*, 2005]. The rate of diffusion and hence crack tip migration should therefore be much lower for adsorbed aqueous films than when liquid brine is present. Very little is known about the thickness and diffusive properties of such fluid films, notably under the humidity conditions relevant for damaged rock salt (i.e., the EDZ) in geological storage systems.

1.3. Present Aims

[10] The objective of this paper is to determine the effective surface diffusivity $S = D\delta C$ for cleavage crack surfaces in NaCl coated with an adsorbed aqueous film, under humidity conditions ranging from almost perfectly dry to the deliquescence point. Our approach employs impedance spectroscopy, whereby the electrical resistance of a thin adsorbed film on the surface of individual salt crystals is isolated from the capacitive or inductive circuit/electrode effects by measuring the total impedance over a wide frequency spectrum. The film resistance values obtained are related to the effective surface diffusivity using the Nernst-Einstein equation, described by *de Meer et al.* [2002].

2. Experimental Methods

[11] In this study, electrical impedance spectroscopy [*MacDonald and Kenan*, 1995; *Barsoukov and Macdonald*,

Table 1. List of Relevant Quantities in the Impedance Spectroscopy Experiment[a]

	Symbol	Units	Value (if Applicable)
Absolute humidity	AH	g m^{-3}	-
Solubility of NaCl	C	m^3 m^{-3}	0.165
Diffusivity	D	m^2 s^{-1}	-
Faraday's constant	F	C mol^{-1}	96485.3399
Length of square electrode	L	m	5.0×10^{-3}
Gas constant	R	J K^{-1} mol^{-1}	8.314472
Relative humidity	RH	%	-
Surface resistance	R_S	Ω	-
Effective surface diffusivity	S	m^3 s^{-1}	-
Temperature	T	K	296 ± 1
Molar volume of solid NaCl	V_m	m^3 mol^{-1}	$2.705683796 \times 10^{-5}$
Complex impedance	Z	Ω	-
Crack geometry parameter	a/b	-	1000
Typical crack tip radius	r	μm	0.5–5
Electrode radii Crystal 1	r_1, r_2	m	0.105, 0.1589
Spacing between square electrodes	w	m	3.0×10^{-3}
Interfacial energy (dry, wet)	γ	J m^{-2}	0.211, 0.129
Fluid film thickness	δ	m	$1–90 \times 10^{-9}$
Crack opening angle	θ	-	≈ 0
Geometric constant crack (dry, wet)	λ	-	δ/r, $b/2$
Geometric constant Crystal 1, 2	$\xi1$, $\xi2$	-	0.06594, 0.3
Resistivity	ρ	Ω m	-
Conductivity	σ	S m^{-1}	-

[a]In case no value is given, the quantity is either measured or calculated in the experiments.

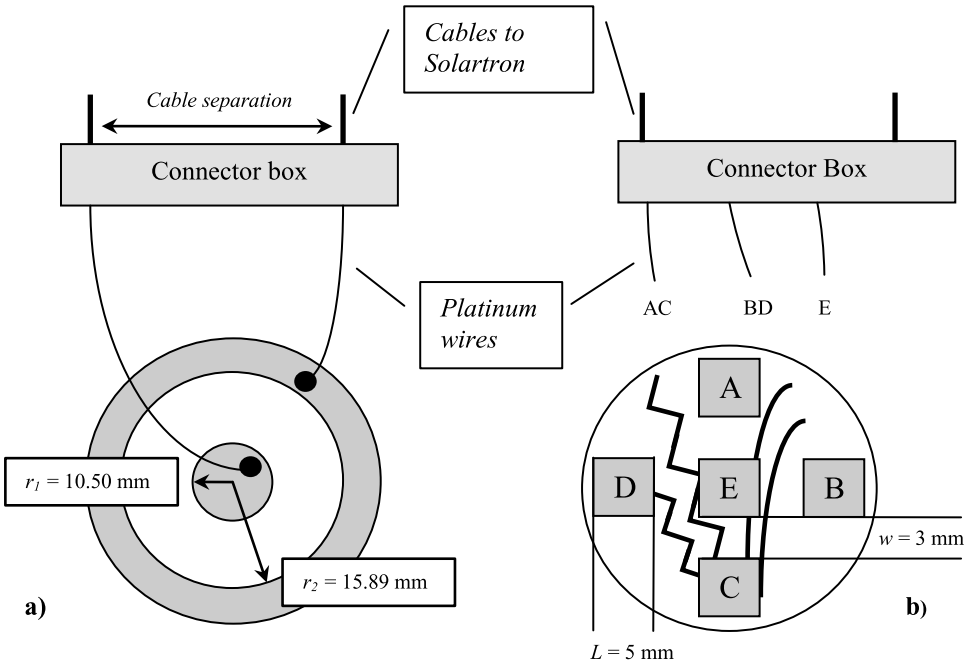

Figure 3. General lay-out of the crystal electrode configurations used in the present experiments. Note that the crystals are nominally 4 mm thick circular discs cleaved from cylindrical cores cut from NaCl crystals. (a) Plan view of Crystal 1 with the concentric electrode configuration characterized by the radii of the electrodes r_1 and r_2. (b) Plan view of Crystal 2 with the square electrode configuration characterized by the spacing w and active length L of the electrodes. Surface cleavage steps on Crystal 2 are sketched using bold lines.

2005] is used to measure the surface impedance of cleaved NaCl crystals carrying an adsorbed water film in equilibrium with a controlled humidity environment. Using this method, the impedance and phase shift characteristics of the crystal surfaces are measured as a function of frequency of an applied sinusoidal voltage, to obtain the resistance (real component) and capacitance [*ten Grotenhuis et al.*, 2004]. Quantitative information regarding the conductance, dielectric coefficient, capacitance, and dynamic changes in these quantities due to adsorption or charge-transfer-phenomena, are obtained by fitting the measured imaginary versus real impedance components. The phase shift can display a strong dependence on the angular frequency, which results in one or more arcs in these complex impedance plots. Characteristic plots of this type allow analysis of the system in terms of equivalent circuit elements. However, many equivalent circuits are possible for a given complex plot, so care must be taken in analyzing the results.

2.1. Theory and Configuration

[12] In the present experiments, two crystals with different electrode configurations were used (Figure 3). Crystal 1 was prepared with a concentric electrode configuration (radii r_1 and r_2, length $2\pi r_n$), whereas Crystal 2 was fitted with multiple square electrodes of effective length L and spacing w (see Table 1 for a list of all relevant parameters with their corresponding values). We assumed that in both situations all electric flux lines directly linked the high- and low-potential electrodes. Conduction occurred through a thin water film adsorbed on the surface of the crystals. For very small thicknesses of this film, we assume that the film conductivity can be treated as a surface conductivity [*Maryniak et al.*, 2003], leading to the following expression for the conductivity of the samples in terms of surface resistance

$$\sigma \equiv \frac{1}{\rho} \cong \frac{1}{\rho_S \delta} = \frac{\xi}{R_S \delta}, \tag{2}$$

where σ is the conductivity, ρ the resistivity, ρ_S the surface resistivity, R_S the surface resistance and δ the thin film thickness. The geometric constant ξ is given for Crystal 1 and Crystal 2, respectively, by (Figure 3)

$$\xi_1 = \frac{\ln(r_2/r_1)}{2\pi} \tag{3}$$

$$\xi_2 = \frac{w}{2L}. \tag{4}$$

We used impedance spectroscopy to obtain the resistance and hence the conductivity of the salt surface. The conductivity and diffusivity are related by the Nernst-Einstein relation, which following the protocol of *de Meer et al.* [2002], can be simplified to

$$\sigma = \frac{2F^2 DC}{RTV_m}. \tag{5}$$

Here F is Faraday's constant, R the gas constant, T the absolute temperature, D the diffusion coefficient of the diffusive species in the adsorbed film, C is the solubility of the

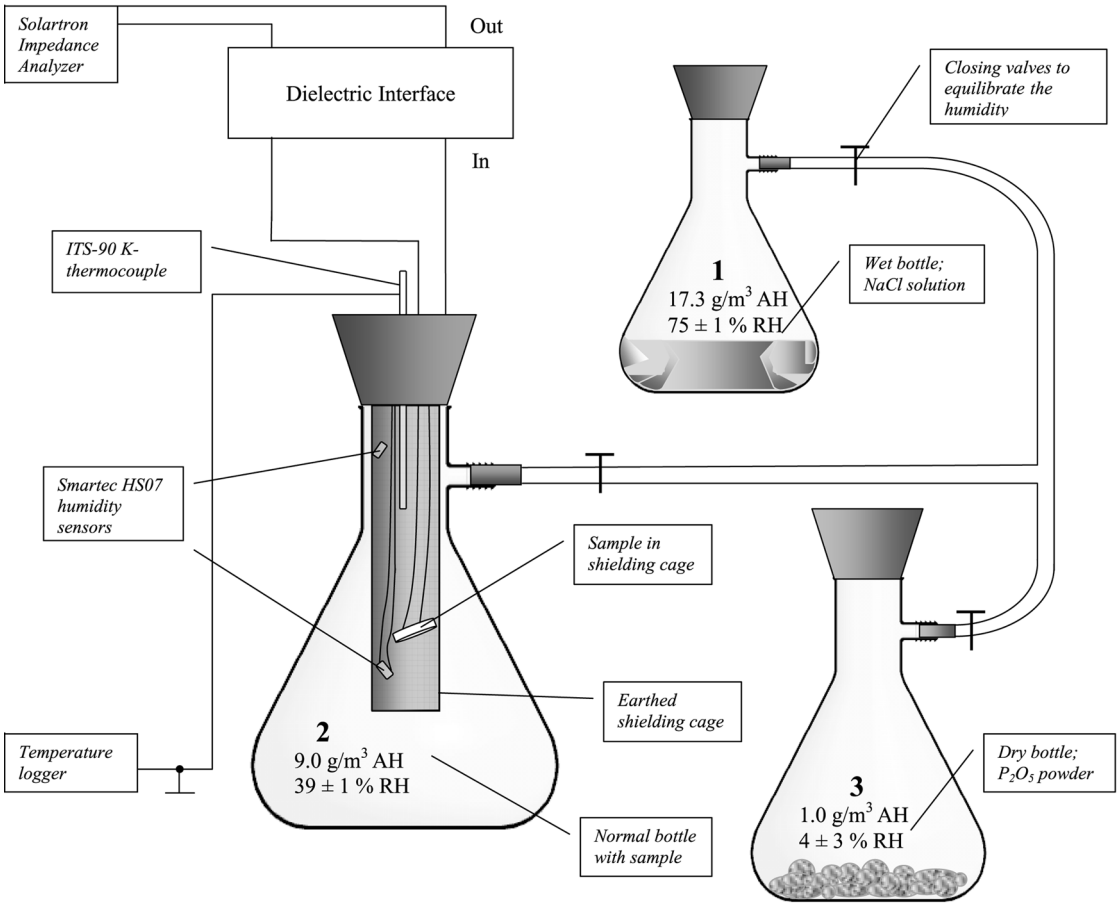

Figure 4. Schematic set-up of the experimental apparatus.

solid in the adsorbed film and V_m is the molar volume of the solid.

[13] Equations (2) and (5) can now be combined to obtain the effective surface diffusivity given:

$$S = D\delta C = \frac{\xi RTV_m}{2R_S F^2}, \tag{6}$$

which includes all unknown parameters, including C and δ.

[14] The values of the constants in (6) and the units of all important quantities are listed in Table 1.

2.2. Sample Preparation

[15] The samples consisted of circular salt disks (Figure 3), with a thickness of ~4 mm cleaved from 25 mm diameter cylinders cored from pure, melt-grown halite crystals cored in the (100) direction. The measured surface was the (100) cleavage plane. For Crystal 1, conduction was measured between two concentric gold ring electrodes, with diameters r_1 of 10.50 ± 0.02 mm and r_2 of 15.89 ± 0.02 mm, sputtered onto the crystal using a circular mask (Figure 3). Crystal 2 served to measure any anisotropy associated with cleavage steps developed on the cleaved surface and to check reproducibility. Five square electrodes with a length of 5 mm were gold-sputtered onto the surface of Crystal 2 with a spacing of 3 mm between them (Figure 3). The center electrode E was used as the high-potential electrode and either A plus C or B plus D served as the low-potential electrodes. Major steps run as indicated in Figure 3. Platinum wires were attached to gold-sputtered electrodes on the surface of the samples using conductive graphite paint.

2.3. Apparatus

[16] The sample was placed together with humidity and temperature sensors inside an earthed aluminum-shielding cage to reduce interference and noise in the data. This was placed in a closed flask system used to control humidity (Figure 4). The impedance measurements were performed using a Solartron 1260 Impedance Analyzer connected to a 1296A Dielectric Interface, which was in turn connected via an electrode connector box to the platinum wires of the sample (Figure 4). The measurements were conducted using an RMS voltage of 100 mV AC, employing frequency sweeps covering the range 100 mHz to 1 MHz at 10 frequency steps per decade using a 10-cycle integration to improve signal-to-noise ratios.

2.4. Humidity Measurement and Control

[17] We used a saturated NaCl solution and dry phosphorous pentoxide (P_2O_5) powder to generate equilibrium relative humidities (RH) at 296 K of 75 ± 1% and 4 ± 3%, respectively, [*Paquette*, 1995; *Lide*, 2000], corresponding to absolute humidities (AH) of 17.3 g/m^3 and 1.0 g/m^3. These humidity buffers were located in Flasks 1 and 3 (Figure 4).

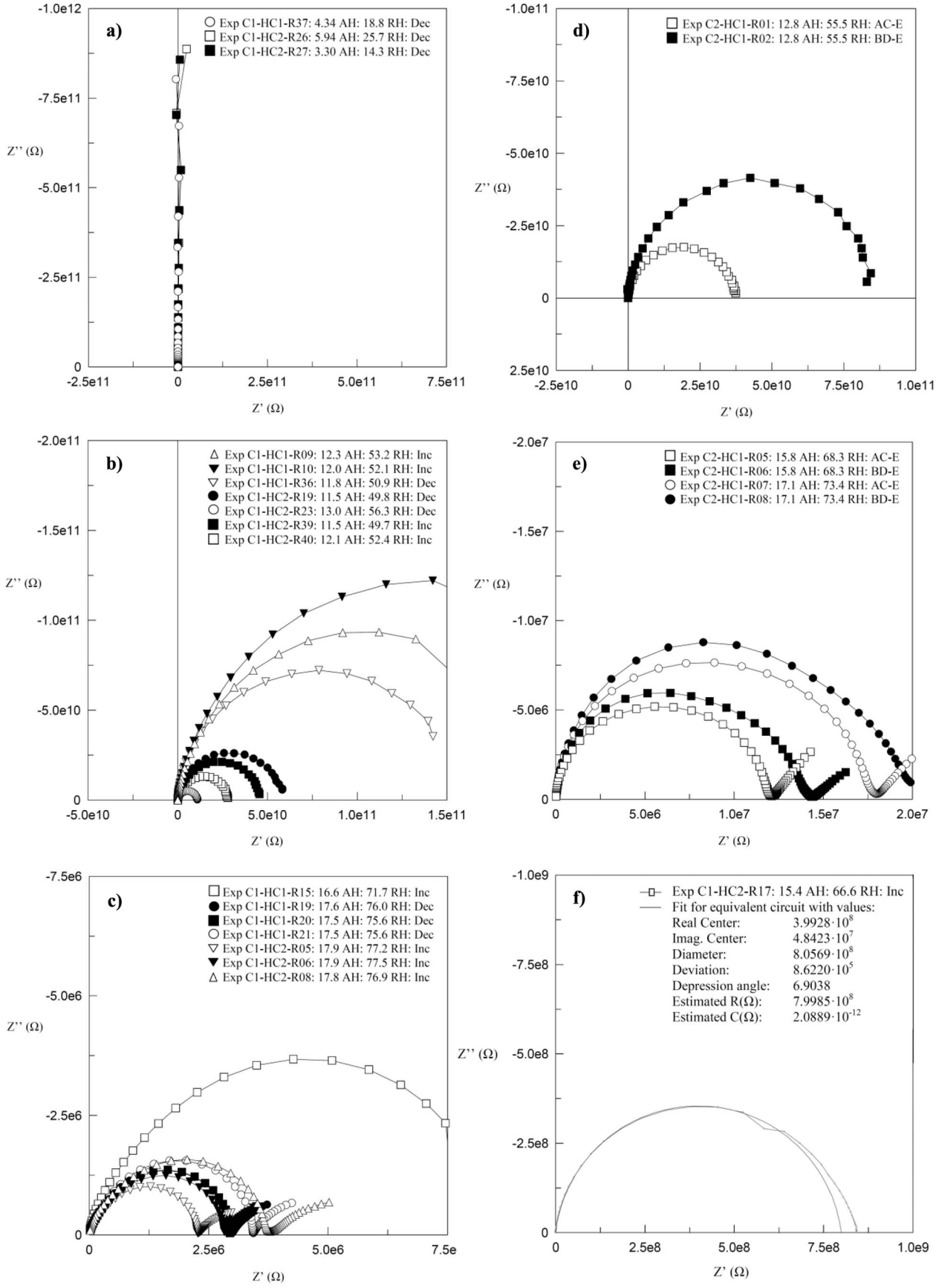
a)
Exp C1-HC1-R37: 4.34 AH: 18.8 RH: Dec
Exp C1-HC2-R26: 5.94 AH: 25.7 RH: Dec
Exp C1-HC2-R27: 3.30 AH: 14.3 RH: Dec
-1.0e12
-7.5e11
-5.0e11
-2.5e11
0
-2.5e11
0
2.5e11
5.0e11
7.5e11
Z'' (Ω)
Z' (Ω)
d)
Exp C2-HC1-R01: 12.8 AH: 55.5 RH: AC-E
Exp C2-HC1-R02: 12.8 AH: 55.5 RH: BD-E
-1.0e11
-7.5e10
-5.0e10
-2.5e10
0
2.5e10
-2.5e10
0
2.5e10
5.0e10
7.5e10
1.0e11
Z'' (Ω)
Z' (Ω)
b)
Exp C1-HC1-R09: 12.3 AH: 53.2 RH: Inc
Exp C1-HC1-R10: 12.0 AH: 52.1 RH: Inc
Exp C1-HC1-R36: 11.8 AH: 50.9 RH: Dec
Exp C1-HC2-R19: 11.5 AH: 49.8 RH: Dec
Exp C1-HC2-R23: 13.0 AH: 56.3 RH: Dec
Exp C1-HC2-R39: 11.5 AH: 49.7 RH: Inc
Exp C1-HC2-R40: 12.1 AH: 52.4 RH: Inc
-2.0e11
-1.5e11
-1.0e11
-5.0e10
0
-5.0e10
0
5.0e10
1.0e11
1.5e11
Z'' (Ω)
Z' (Ω)
e)
Exp C2-HC1-R05: 15.8 AH: 68.3 RH: AC-E
Exp C2-HC1-R06: 15.8 AH: 68.3 RH: BD-E
Exp C2-HC1-R07: 17.1 AH: 73.4 RH: AC-E
Exp C2-HC1-R08: 17.1 AH: 73.4 RH: BD-E
-2.0e7
-1.5e7
-1.0e7
-5.0e6
0
0
5.0e6
1.0e7
1.5e7
2.0e7
Z'' (Ω)
Z' (Ω)
c)
Exp C1-HC1-R15: 16.6 AH: 71.7 RH: Inc
Exp C1-HC1-R19: 17.6 AH: 76.0 RH: Dec
Exp C1-HC1-R20: 17.5 AH: 75.6 RH: Dec
Exp C1-HC1-R21: 17.5 AH: 75.6 RH: Dec
Exp C1-HC2-R05: 17.9 AH: 77.2 RH: Inc
Exp C1-HC2-R06: 17.9 AH: 77.5 RH: Inc
Exp C1-HC2-R08: 17.8 AH: 76.9 RH: Inc
-7.5e6
-5.0e6
-2.5e6
0
0
2.5e6
5.0e6
7.5e
Z'' (Ω)
Z' (Ω)
f)
Exp C1-HC2-R17: 15.4 AH: 66.6 RH: Inc
Fit for equivalent circuit with values:
Real Center: 3.9928·10^8
Imag. Center: 4.8423·10^7
Diameter: 8.0569·10^8
Deviation: 8.6220·10^5
Depression angle: 6.9038
Estimated R(Ω): 7.9985·10^8
Estimated C(Ω): 2.0889·10^-12
-1.0e9
-7.5e8
-5.0e8
-2.5e8
0
0
2.5e8
5.0e8
7.5e8
1.0e9
Z'' (Ω)
Z' (Ω)

Figure 5

The humidity was measured in the flask containing the sample using two Smartec HS07 capacitance sensors with 2% linearity and a sensitivity of 0.6 ± 0.05 pF / % RH connected to the Solartron Analyzer. Both sensors were calibrated using equilibrium humidity values of the NaCl saturated solution and the P_2O_5 powder.

[18] The sensors, located at different positions inside the shielding cage, responded quickly and consistently to all changes in humidity. Temperature was constant at 296 ± 1 K inside and outside the measurement flask and was measured using a K-type thermocouple and a mercury thermometer respectively. We observed no effect of temperature on humidity.

2.5. Experimental Procedure and Open Cell Measurements

[19] The impedance of each sample was first measured at normal atmospheric reference conditions in Flask 2 with all valves closed (9 g/m^3 AH, 39% RH). The sample was subsequently exposed to different humidities by connecting Flask 1 or 3 to Flask 2, or by placing the sample in Flasks 1 or 3 to achieve extreme humidities. After each change in humidity, the sample was left to re-equilibrate until the humidity was constant. The impedance across the surface of the sample was then measured in multiple frequency sweeps. The humidity was continuously measured before and after each impedance run.

[20] For Crystal 1, the humidity was varied between the maximum and minimum values accessible, in two full up-down cycles. For Crystal 2, one humidity cycle was performed. At each humidity investigated, the impedance across electrode directions AC-E and BD-E was measured.

[21] To check for unexpected apparatus effects, we measured the impedance of the system without the sample present (open cell) at a range of different humidities. The wire configuration with the lowest open cell capacitance (largest separation between the platinum wires at the connector box to the Solartron system) was used for sample measurements. The corresponding open cell capacitance was 0.44 pF, which lies at the limit of the apparatus.

[22] Open cell impedance runs at different humidities showed that the open cell capacitance changed only slightly and had an average value of 1.5 pF. The phase angle was generally close to 90°, suggesting that the open cell behaved as a pure capacitor, although at very low frequencies (below 1 Hz), the phase angle decreased to approach 0° under humid conditions. This behavior seen at low frequencies is believed to be related to the effects of percolation phenomena influencing the connectivity of water adsorbed on the cables connection the sample to the Solartron [*Enapu and Jonscher*, 1987].

3. Results

[23] Eighty-seven impedance runs were conducted on Crystal 1 and five on Crystal 2 at varying humidity conditions. Figure 5 shows representative complex impedance plots of these runs, grouped according to their corresponding humidity value. Characteristic values are given in Table 2.

3.1. Crystal 1

[24] From Table 2 and Figure 5, it is seen that the impedance decreases with increasing humidity. At the lowest humidities measured (~3 g/m^3 AH or 13% RH), the impedance shows pure capacitive behavior characterized by vertical lines with impedance magnitude reaching around 8×10^{11} Ω at low frequencies (Figure 5a). This indicates a very minor dielectric loss and any real (conductive) impedance is well in excess of 10^{13} Ω (to beyond the capabilities of the impedance analyzer). Due to this purely capacitive behavior, these measurements reflect insulative behavior of the experimental cell where no surface conduction occurs, comparable to testing of a standard material. With increasing humidity, the vertical lines evolve into arcs with increasing curvature and impedance magnitudes of 5×10^{10} Ω (Figure 5b). These arcs become fully developed at ~16 g/m^3 AH (69% RH) and approach the real axis at values of 2–4 $\times 10^8$ Ω. At the maximum humidity investigated of 17.9 g/m^3 AH (77.5% RH), the deliquescence point of NaCl, the full arcs cut the real axis at 2–4 $\times 10^6$ Ω (Figure 5c), and they display the beginnings of a second arc or line [*Roberts and Tyburczy*, 1993].

[25] The values obtained under decreasing and increasing humidity conditions are very similar in these runs, showing that the adsorption process is reversible. In addition, the experiment reproducibility is good as runs performed in the second humidity cycle yielded similar results to the first (compare run C1-HC2-R08 and C1-HC1-R21 in Figure 5c).

[26] The most remarkable feature of the results is the large difference in impedance magnitude between the plots. This changes by 6 orders of magnitude across a humidity range of around 4 g/m^3 to 18 g/m^3 absolute humidity (12%–78% relative humidity at 296 K), demonstrating that increasing conduction occurs in the system toward high humidities.

3.2. Crystal 2

[27] The results for Crystal 2 show similar impedance magnitudes to Crystal 1 with impedance values decreasing consistently with increasing humidity (Figure 5). For intermediate humidity conditions (Figure 5d), almost full arcs are observed, approaching the real axis at approximately 10^{10} Ω. For higher humidities (Figure 5e), the impedance amplitude

Figure 5. Complex impedance plots obtained at varying humidity conditions indicated by the humidity cycle (HC) and run number (R). AH indicates the absolute humidity value (g/m^3) and RH the relative humidity value (%). Dec or Inc denotes increasing or decreasing humidity for Crystal 1 and AC-E and BD-E indicate the direction of measurement for Crystal 2. Surface resistance data for Crystal 1 for (a) the lowest humidities of 1–8 g/m^3 AH (4%–35% RH); (b) intermediate humidities of 8–14 g/m^3 AH (35%–60% RH) and (c) the highest humidities of 14–18 g/m^3 AH (60%–78% RH). Total surface resistance data for the parallel electrodes of Crystal 2 for in (d) intermediate humidities of 12.78 g/m^3 AH (55.5% RH) and (e) high humidities of 16–17 g/m^3 AH (68%–74% RH). (f) Complex impedance plot for Crystal 1 showing the fit of the equivalent circuit to the data. Note the change in impedance behavior from a pure imaginary capacitive component at low humidities to the development of clear arcs (implying a mixed capacitive and resistive behavior) at intermediate humidities, and ultimately to fully developed arcs with the development of second arcs at high humidities.

Table 2. Overview of the Most Important Quantities Measured[a]

	Absolute Humidity 1–8 (g/m^3)	Absolute Humidity 8–14 (g/m^3)	Absolute Humidity 14–18 (g/m^3)
Relative humidity (%)	4–35	35–60	60–78
Typical impedance amplitude (Ω)	8×10^{11}	5×10^{10}	8×10^{6}
Surface resistance (Ω)	2×10^{14}–1×10^{13}	2×10^{13}–9×10^{9}	2×10^{9}–2×10^{6}
Effective surface diffusivity (m^3 s^{-1})	1×10^{-27}–3×10^{-26}	1×10^{-26}–3×10^{-23}	1×10^{-22}–1×10^{-19}
Assumed thickness (nm)	1–10	10–50	50–90
Diffusivity (m^2 s^{-1})	1×10^{-18}–1×10^{-17}	2×10^{-17}–4×10^{-15}	1×10^{-14}–8×10^{-12}

[a]The results are grouped into three humidity ranges and typical values are given to demonstrate the general trends.

is $\sim 10^7$ Ω with no significant difference between the two directions measured. Second arcs or lines also appear. For all humidities, it should be noted that the values obtained for direction BD-E are lower than for direction AC-E by a factor of 2. The points where the arcs approach the real axis (the resistance values) are slightly higher for Crystal 2 than Crystal 1. Note, however, that the resistance values cannot be directly compared because they are related to different electrode configurations and that the values plotted are the total measured parallel resistance instead of the individual surface resistance of the two parallel electrode paths.

3.3. Other System Characteristics

[28] In Figure 6 we show the relative permittivity for intermediate and high-humidity conditions. The relative permittivity was related to the capacitive components in the electrical impedance analysis. The relative permittivity was constant within 1 order of magnitude except at high-humidity runs where it changed by approximately 4 orders of magnitude at frequencies between 100 mHz and 100 Hz. This behavior is likely to be due to the charging of the electrodes by the formation of a capacitive Gouy-Chapman type double layer of water molecules and ions [*Roberts and Tyburczy*, 1993; *Orazem and Tribollet*, 2008].

4. Data Analysis

[29] The effective surface diffusivity for conduction on the salt surface can be obtained using equation (6) plus the measured value of circuit resistance. To obtain this from the complex impedance plots, we interpreted the high-frequency arcs observed in the complex plane as resulting from an electric circuit consisting of a parallel resistor and capacitor. This single arc fitting is justified as the appearance of the second arcs toward low frequencies under high-humidity conditions is also accompanied by rapid increases in frequency-dependent capacitance causing some arc depression and signs of low-frequency dispersion as described by *Jonscher* [1991]. The high-frequency arcs exhibit good semicircular form with frequency-independent capacitance over the complete humidity range. Hence, these arcs are interpreted to be purely the effect of surface conduction in parallel with a constant capacitance.

[30] All impedance results were fitted to the above circuit model to yield the surface resistance for each run. To account for arc distortion at low frequencies we only fitted the high-frequency arcs for which the permittivity was constant within 1 order of magnitude. In Figure 5f we show a typical fit of the equivalent circuit to the complex impedance data for Crystal 1 at 15.4 g/m^3 AH. The corresponding relative permittivity for this run is shown in Figure 6b where we indicated the frequency range included in the fit. In addition, we neglected the open cell contribution, as those impedance values were 6 orders of magnitude higher than those of the crystals.

4.1. Surface Resistance

[31] The combined results of the arc fitting procedure for Crystals 1 and 2 are presented in Table 2 and Figure 7, where the log of surface resistance is plotted versus humidity. Error bars for humidity are plotted, reflecting errors in the calibration, which range from 3 g/m^3 at low humidities to 0.9 g/m^3 at high humidities. Errors in resistance resulting from the fitting procedure were generally < 0.5% of the corresponding value.

[32] Two regimes are visible in the resistance plot. At low humidities (1–5 g/m^3 AH, 4–25% RH), the log of the resistance is more or less constant under decreasing humidity conditions reflecting a resistance of $\sim 10^{13-14}$ Ω. At

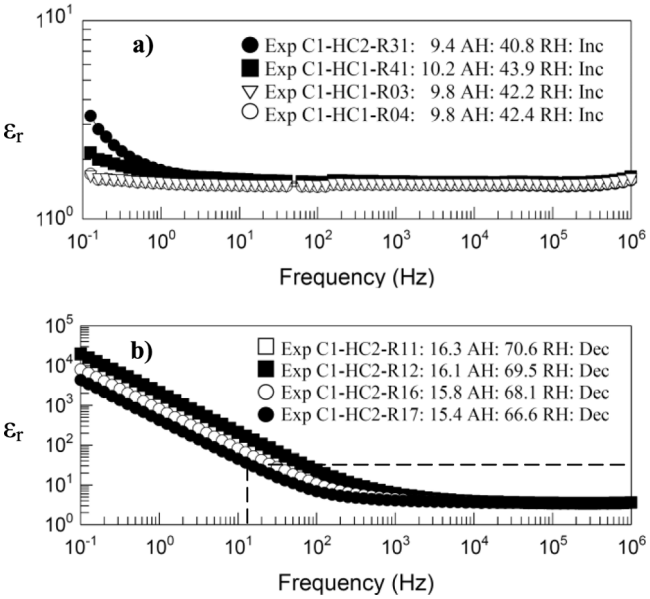

Figure 6. Plots of relative permittivity magnitude versus frequency obtained at (a) intermediate humidity conditions of ~ 10 g/m^3 AH (41%–44% RH) and (b) high humidities of ~ 16 g/m^3 AH (68%–71% RH). The measurements are identified as indicated by the humidity cycle number HC and run number R as in Figure 5. For intermediate humidities, the permittivity values fall within 1 order of magnitude whereas for higher humidities, the permittivity diverges significantly at low frequencies. Dashed lines indicate the frequency range used in the fit for Figure 5f, e.g., where the permittivity changes less than 1 order.

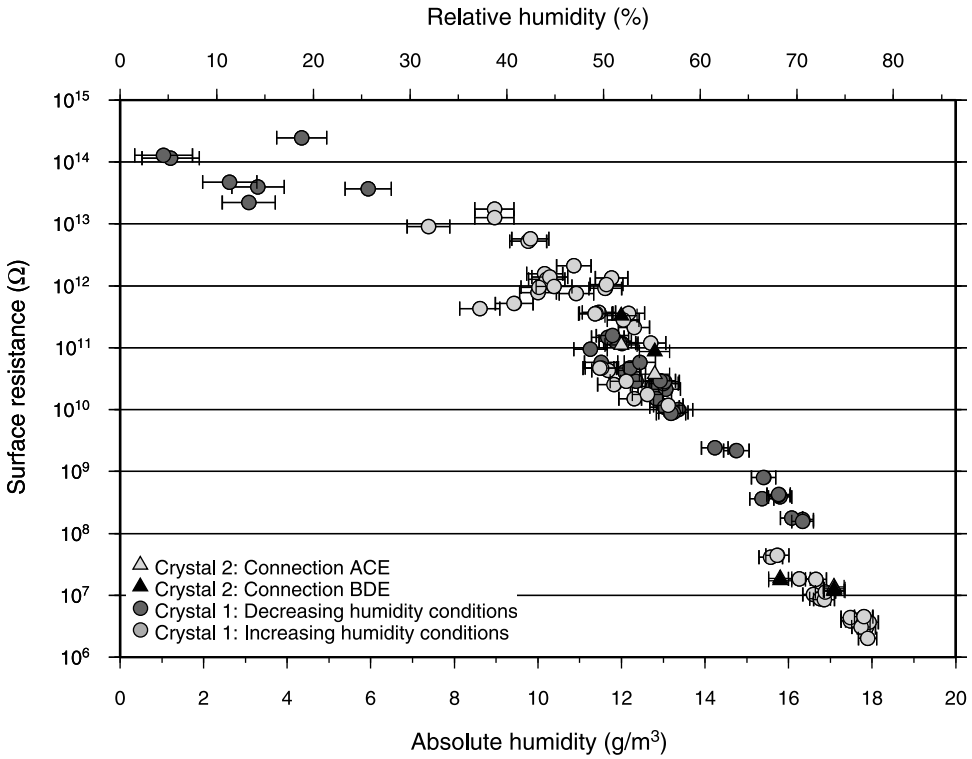

Figure 7. Plot of the log of resistance versus absolute and relative humidity (at 296 K) for Crystal 1 (circles) and Crystal 2 (triangles). The values for increasing (light circles) and decreasing (dark circles) humidity conditions are shown for Crystal 1. For Crystal 2, the total parallel surface resistance data are displayed separately for directions AC-E (light triangles) and BD-E (dark triangles). Errors in humidity are represented by the bars shown. Errors in resistance are less than 0.5% of the corresponding value, i.e., smaller than the data points plotted. The resistance is roughly constant up to 8 g/m^3 AH (35% RH) before rapidly decreasing by 7 to 8 orders of magnitude. Note the similarity of the results for both crystals.

humidities above ~8 g/m^3 AH (26%–35% RH), however, the log of resistance decreases steadily implying absolute resistances around 2×10^6 Ω for humidities near the deliquescence point at 18 g/m^3 AH (78% RH). Overall, the resistance changes by 8 orders of magnitude across the humidity range investigated.

[33] Note that the measurements for increasing and decreasing humidity conditions plot as different parallel trends with a small offset relative to each other of about 1 order of magnitude. The difference in values between the two crystals is also relatively small. At the intermediate humidities, the resistances measured for Crystal 2 are twice as large for direction BD-E compared to direction AC-E, suggesting more conduction parallel to the cleavage steps. However, there is no significant difference for the two directions at higher humidities. The scatter observed in the data is independent of the measurement uncertainties, but merely reflects the variability in resistance due to the dynamics of the salt surface.

4.2. Effective Surface Diffusivity

[34] The effective surface diffusivity S was obtained using equation (6). The resulting data is plotted versus humidity in Figure 8. Characteristic values are given in Table 2 for three humidity ranges. The errors in the effective surface diffusivity have been determined using standard error propagation theory [*Lindberg*, 2000], considering the errors in S to be caused by errors in three independent variables: the geometric constants of the samples, the temperature T and the resistance value R_S. This resulted in errors in S of $\pm$ 3.1 $\times 10^{-29}$ m^3 s^{-1} at low humidities up to $\pm$ 4.2 $\times 10^{-21}$ m^3 s^{-1} for high humidities, i.e., less than $\pm$ 4% of the corresponding value.

[35] At humidities lower than 8 g/m^3 (35% RH), the effective surface diffusivity has an average value of ~1 $\times 10^{-27}$ m^3 s^{-1} and it increases up to 1×10^{-19} m^3 s^{-1} for absolute humidities of 18 g/m^3 (78% RH). The values for Crystal 2 are slightly larger than those for Crystal 1. However, these differences are small compared to the total change with humidity, which increases our confidence that the values obtained for diffusion over the (100) salt surface are not significantly dependent on the electrode configuration used.

5. Discussion

5.1. Comparison With Previous Work

[36] The values for resistance (10^{14} to 2×10^6 Ω) that we obtained in this study using impedance measurements on single salt crystals at humidities ranging from 1 to 18 g/m^3 absolute humidity (4%–78% RH, given in Table 2) are in reasonable agreement with those derived from scanning polarizing force microscopy, pressure solution creep experiments on NaCl aggregates and single contact pressure solution experiments. Conductivity experiments performed by

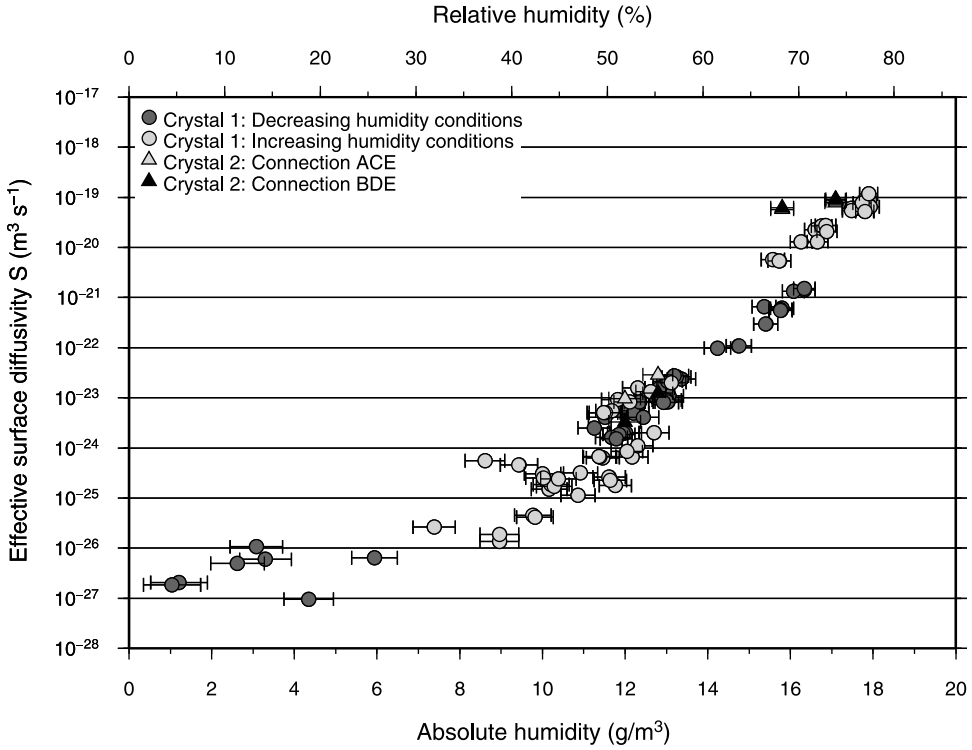

Figure 8. Plot of the log of effective surface diffusivity S ($D\delta C$) versus absolute humidity and relative humidity at 296 K. Symbols and error bars are as in Figure 7 with errors in S less than 4% of the corresponding value. The effective surface diffusivity starts to rise quickly beyond an absolute humidity of 8 g/m^3 (35%–40% RH).

Simkovich [1963] (along cleaved halite rods) and *Hucher et al.* [1967] (across cleaved halite cubes), using similarly dimensioned electrode configurations show very similar resistances with values in the range 10^{11}–10^8 Ω and 10^{14}–10^6 Ω, respectively, for similar, but unspecified, humidity values. Using a scanning polarizing force microscopy method, *Luna et al.* [1998] obtained resistance values of 2×10^{12} to 2×10^8 Ω for humidities of 33% to 60% RH, which are also consistent with the values measured in the present study.

[37] The values of the effective surface diffusivity S ($D\delta C$) derived in the present experiments (1×10^{-27} m^3 s^{-1} to 1×10^{-19} m^3 s^{-1}) span a large range as a function of humidity. As far as we are aware, it is the first time that S values have been derived for adsorbed films in the absence of liquid brine. Therefore, we can only compare our values measured at high humidities, i.e., the deliquescence point around 18 g/m^3 AH (78% RH) (1×10^{-20} m^3 s^{-1} to 1×10^{-19} m^3 s^{-1}), with previous determinations performed by means of experiments on wet NaCl. *Spiers et al.* [1990] obtained values of S in the range 6×10^{-20} m^3 s^{-1} to 2×10^{-19} m^3 s^{-1} for thin intergranular brine films at a temperature of 297 K in pressure solution creep experiments on granular NaCl aggregates. From diffusion controlled pressure solution occurring in brine-wetted glass-halite contacts, *Hickman and Evans* [1995] inferred values for S in a similar range (4×10^{-20} m^3 s^{-1} to 2×10^{-19} m^3 s^{-1}). *Spiers and Schutjens* [1999] obtained values for the effective grain boundary diffusivity between 5×10^{-20} m^3 s^{-1} to 5×10^{-19} m^3 s^{-1} using similar contact dissolution experiments on single halite-halite and halite-glass contacts. In more recent experiments [*de Meer et al.*, 2002] radial resistance was measured for halite-glass contacts undergoing active pressure solution, yielding values of S in the range 3×10^{-20} – 5×10^{-19} m^3 s^{-1} for brine filled grain boundaries. By contrast, *de Meer et al.* [2005] obtained values between 1×10^{-18} m^3 s^{-1} to 3×10^{-18} m^3 s^{-1} for NaCl-CaF_2 contacts undergoing active pressure solution of the NaCl. These values are 1 order of magnitude higher than most experiments including our own. This probably reflects the development of thick fluid films on the charged (111) NaCl surface dissolved in those experiments.

[38] Overall, the values of our calculated effective surface diffusivity for the high humidities lie in the same range as those given previously for the effective diffusivity of fully wetted grain boundaries. This suggests that our samples behaved as if they were coated with a saturated brine film of similar thickness to that present in grain boundaries undergoing pressure solution. At lower humidities, however, effective surface diffusivities are clearly much lower, implying lower values, not only of film thickness but also possibly lower values of D or even C. This has important implications for diffusive transport in salt under dry geological storage conditions.

5.2. Structure and Thickness of the Adsorbed Fluid Film

[39] Several studies have focused on the structure of adsorbed water films on the surface of NaCl. These studies, which include theoretical considerations [*Barraclough and*

Hall, 1974; *Shinto et al.*, 1998; *Foster and Ewing*, 2000], scanning probe microscopy measurements [*Dai et al.*, 1997; *Luna et al.*, 1998], electron spectroscopy experiments [*Fölsch and Henzler*, 1991], and infrared measurements [*Barraclough and Hall*, 1974; *Peters and Ewing*, 1997a, 1997b; *Foster and Ewing*, 1999; *Foster and Ewing*, 2000] show the following three-stage picture. At low humidities, isolated, monolayered patches of water molecules develop on the surface. Slow, linear growth of coverage with humidity causes these to become progressively more linked, leading to the development of two-dimensional (2-D) network structures, the conductivity of which is governed by percolation phenomena. At higher humidities, ongoing adsorption forms 3-D networks of hydrogen-bonded water molecules configured in a tetrahedral arrangement [*Ewing*, 2005, 2006]. The humidity at which the transition from two-dimensional coverage to three-dimensional coverage has been inferred to occur, varies from 28% RH [*Peters and Ewing*, 1997a, 1997b] to 35% RH [*Barraclough and Hall*, 1974; *Dai et al.*, 1997] to 46% RH [*Luna et al.*, 1998] and corresponds to a sharp increase in water coverage with humidity [*Foster and Ewing*, 1999]. At high humidities, i.e., beyond 60% RH, coverage increases more slowly again with humidity. In this regime, it is believed that the hydrogen-bonded network assumes a structure resembling that of liquid water, and that the fluid film behaves increasingly like a saturated NaCl solution [*Foster and Ewing*, 2000].

[40] Comparison of these reported trends with our measurements suggests that the change in slope observed near an absolute humidity of ~8 g/m^3 (39% RH at 296 K) (Figures 7 and 8) is related to the change in the nature of water adsorbance from 2-D networks to 3-D tetrahedral arrangements. Noting the log linear nature of Figure 8, our high-conductance values in the range 14–18 g/m^3 AH (60%–78% RH) can be explained by the fluid film progressively acquiring the properties of a saturated solution, as proposed by *Foster and Ewing* [2000] and *Barraclough and Hall* [1974]. The possibility exists that conduction along cleavage steps, where the fluid film thickness may be larger [*Luna et al.*, 1998], influences our results. However, the measurements on Crystal 2 suggest that anisotropy is only significant at low humidities, presumably due to preferential water adsorption at steps and edges [*Dai et al.*, 1997; *Luna et al.*, 1998], whereas at higher humidities water coverage is sufficient to allow isotropic conduction.

[41] Estimates of the thickness of the adsorbed water film have been made from atomic force microscopy observations [*Dai et al.*, 1997] and infrared spectroscopy measurements [*de Meer et al.*, 2005]. These yield mean values of 10–50 nm at an RH of 35%–60% [*Dai et al.*, 1997] versus values of 85–185 nm at high humidities where liquid brine is present [*de Meer et al.*, 2005]. Values in the range of 0.1–0.5 nm have been inferred for very low humidities [*Ewing*, 2006].

5.3. Diffusivity in Thin Fluid Films

[42] To gain insight into the thickness and humidity dependence of the intrinsic diffusivity D of the fluid film, we now calculate D from $S = D\delta C$, assuming a constant solubility C and a humidity-dependent thickness δ based on the above literature values. This approach is expected to be valid at least for humidities > 14 g/m^3 (>60% RH), where a 3-D liquid-like water structure is present. Since the adsorption behavior of water on NaCl does not obey a classical adsorption isotherm or coverage-humidity function [*Foster and Ewing*, 2000], we assume three different (piecewise linear) ranges for the thickness δ of the fluid film in the three inferred humidity/structure regimes (Table 2 and Figure 9a). For low absolute humidities of 1–8 g/m^3 (4%–35% RH), a thickness of 1–10 nm is assumed in line with the study of *Ewing* [2006] and *Dai et al.* [1997]. At intermediate humidities (8–14 g/m^3 AH or 35%–60% RH), we assume a water layer thickness of 10–50 nm consistent with the work of *Dai et al.* [1997] and *Watanabe and Peach* [2002]. For high-absolute humidities (higher than 14 g/m^3 AH or 60% RH), where a hydrogen-bonded structure similar to liquid water is believed to be present, we assume a thickness of 50–90 nm [c.f. *Dai et al.*, 1997; *de Meer et al.*, 2005].

[43] Values computed for the diffusivity D, assuming the film thickness values above (Figure 9a) along with a solubility C of NaCl of 0.165 m^3 m^{-3} appropriate for bulk NaCl solution at room temperature [*de Meer et al.*, 2005], are presented in Figure 9b. Sensitivity analysis has shown that the results are barely affected by choosing either an exponential or power law fit to the thickness-humidity constraints upon which our piecewise linear description of Figure 9a is based. The values obtained for D vary between 1×10^{-18} m^2 s^{-1} and 8×10^{-12} m^2 s^{-1} (Table 2). Using electrical impedance measurements on recrystallized polycrystalline samples containing 30 ppm water, *Watanabe and Peach* [2002] calculated values for D of $8 \times 10^{-(14\ \text{to}\ 12)}$ m^2 s^{-1}. *de Meer et al.* [2002] obtained diffusivities of 8.7×10^{-11} – 1.0×10^{-10} m^2 s^{-1} for NaCl-glass contacts undergoing pressure solution of NaCl. Both are in reasonable agreement with our values for the diffusivity at high humidities, i.e., 14–18 g/m^3 AH (60%–78% RH as given in Table 2). However, even the highest diffusivities that we obtained are 2 orders of magnitude lower than documented values for the diffusivity in bulk solution ($\sim 1 \times 10^{-9}$ m^2 s^{-1} for Na^+ and Cl^- [*Lide*, 2000]) and 5 orders lower at 14 g/m^3 AH (60% RH). This strongly supports the idea that the diffusivity in thin water film is reduced by several orders of magnitude [*Rutter*, 1983; *Nakashima*, 1995]. No previous data are available for comparison with our results for D at lower humidities, as our study if the first to report effective diffusivities at such humidity values. Moreover, at humidities below 14 g/m^3 AH (60% RH), it is questionable whether the adsorbed film has sufficiently liquid-like properties, whether our assumed value of C is valid, whether the film thickness is well-enough constrained, and whether the 3-D or 2-D connectivity of the film is sufficient, for our calculated D values (Figure 9b) to be quantitatively meaningful.

[44] Even at high humidities, i.e., 14–18 g/m^3 AH (60%–78% RH), where liquid-like (water/brine) films exist, uncertainties in our results for D arise from the assumed fluid film thicknesses and solubility value. However, it is highly unlikely that these could lead to more than 1 order of magnitude error in D. The anisotropy in the system due to the influence of cleavage steps could affect the values obtained but in our study this effect is less than a factor of two. Future research should aim to provide more robust constraints on the thickness of the fluid film and on the influence of cleavage steps. In the meantime, the values of effective surface

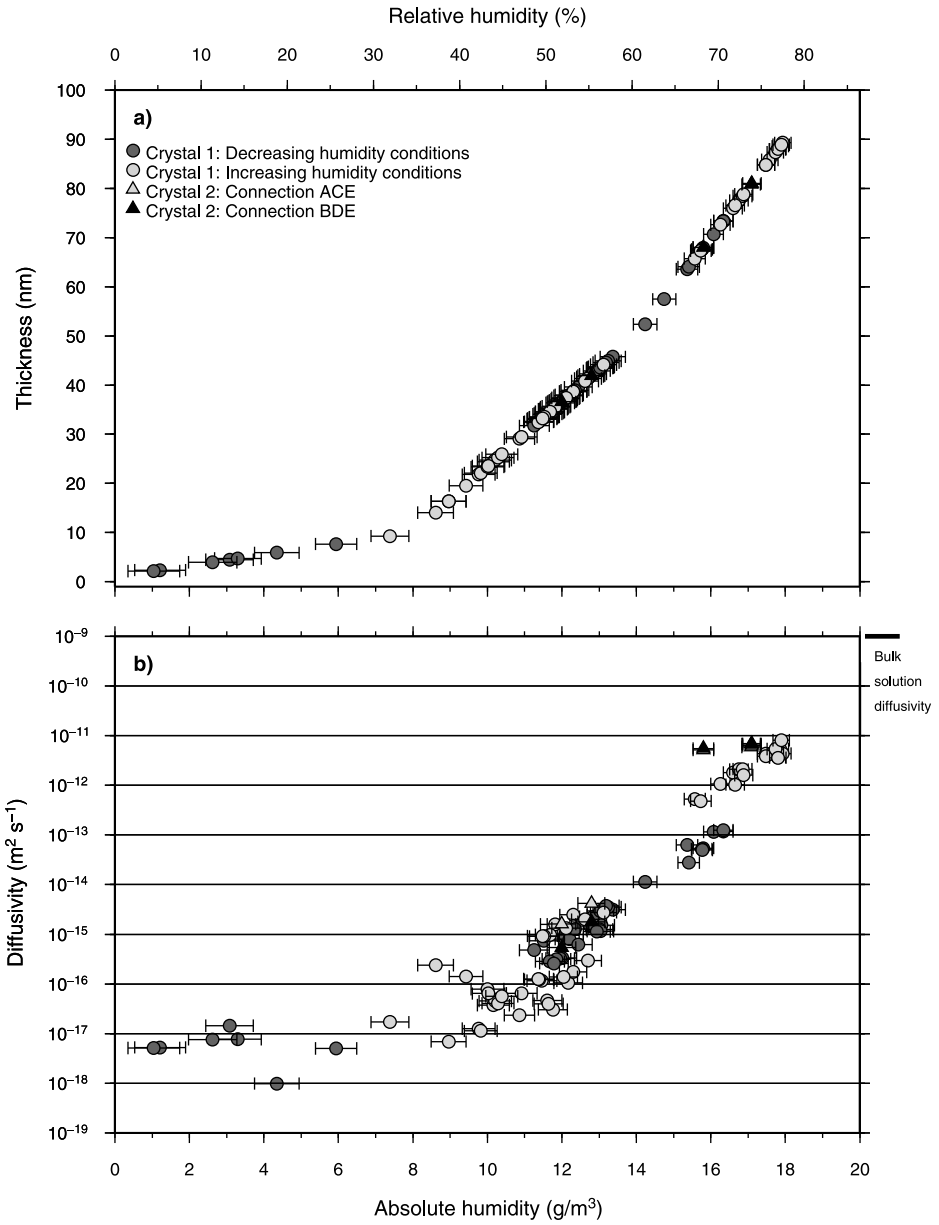

Figure 9. (a) Assumed fluid film thickness and (b) resulting log diffusivity versus humidity plots at 296 K, constructed assuming piecewise linear thicknesses of the adsorbed fluid film in three regions. Symbols and error bars are given as in Figure 7. Uncertainties in assumed thicknesses and solubility are up to 1 order of magnitude, which is small compared to the total variation of diffusivity of ~7 orders of magnitude over the full humidity range.

diffusivity ($S = D\delta C$) measured here are all that is needed to evaluate diffusive mass transport rates in thin adsorbed films as a function of humidity.

5.4. Implications for Geological Storage

[45] Our results for the effective surface diffusivity S have been obtained at room temperature (296 ± 1 K) and absolute humidities up to 18 g/m^3, i.e., up to 78% relative humidity. In rock salt–based geological storage systems at depths up to a few km, it is expected that small quantities of brine naturally present in the salt will buffer the humidity to maximum values relatively close to the deliquescence point (78% RH). On the basis of our findings, we estimate that the most likely range for S in such environments is $1 \times 10^{-22} - 8 \times 10^{-18}$ m^3 s^{-1}, spanning the range from humidities of 14 g/m^3 AH (60% RH) to the bulk solution equivalent taken from the literature. This would correspond to values of $1 \times 10^{-14} - 1 \times 10^{-9}$ m^2 s^{-1} for the diffusivity D, assuming that C is 0.165 m^3 m^{-3} and taking δ as 50–90 nm for the high-humidity data, as shown in Figure 9a.

[46] Our findings accordingly suggest that the diffusion coefficient can be as high as the bulk solution value when

fully buffered by free brine, but may be 2 to 5 orders of magnitude lower for open cracks with thin adsorbed water films under drier conditions. To estimate crack tip migration velocities v for a brine-filled crack at room temperature we will now apply equation (1). We assume a near-parallel crack-wall-geometry defined in terms of $\cos(\theta/2) \approx 1$ and a typical crack width for dilated salt of 1–10 μm [*Peach and Spiers*, 1996], i.e., a crack tip radius of 0.5 to 5 μm. For such a crack geometry, assuming that the crack length will be of the order of the grain size d (typically 2–20 mm for natural salt), then the characteristic transport distance ar will be roughly $d/2$ while the cross section for diffusion br will be approximately equal to $2r$. The ratio $a/b = d/4r$ will accordingly be of the order of 1000 for a given crack porosity [*Peach and Spiers*, 1996] with $a = d/2r = 2000$ and $b = 2$. Further, we take $\gamma = 0.129$ J m^{-2}, calculated following *Israelachvili* [1992] using the data for NaCl given by *Benson and Yun* [1967] and *Gel'perin et al.* [1969]. Equation (1) then predicts a crack tip migration velocity v of $1.5 \times 10^{-5} - 1.5 \times 10^{-7}$ m s^{-1} for crack tip radii of 0.5 and 5 μm, respectively, using a bulk solution value for D of 1×10^{-9} m^2 s^{-1} [e.g., *Nakashima*, 1995].

[47] For a crack whose walls are coated with a 50 nm thick adsorbed aqueous film (δ = 50 nm), again taking $a = 2000$ (in line with $a/b = d/4r = 1000$) and $\gamma = 0.211$ J m^{-2} (the sum of the fluid-vapor and solid-vapor surface energies [*Ozdemir et al.*, 2009]), equation (1) together with our data for $D\delta C$ lead to a migration velocity range of $2.4 \times 10^{-11} - 2.4\ 10^{-14}$ m s^{-1} for a diffusivity value of 1×10^{-14} m^2 s^{-1}. The implication is that the time taken for cracks in rock salt to shrink to the point at which they start to disconnect or neck down, and therefore render the salt impermeable, will likely scale by similar amounts. For example, if we consider grain boundary cracks in rock salt with grain size 5–10 mm, then a contraction of 0.5–2.0 mm should be sufficient to disconnect most cracks. Applying our model for brine filled cracks, this would take only 34 s to 3 h 44 min at room temperature. However, for cracks coated with adsorbed water, this time would be increased to 0.7 to 2600 years. If in situ humidities are lower than 14 g/m^3 (60% RH at room temperature), crack disconnection would take even longer. Future modeling studies should incorporate our values of S as a function of humidity (Figure 7) to more rigorously evaluate healing times in EDZ's associated with geological storage systems in rock salt.

6. Conclusions

[48] We have conducted electrical impedance measurements on the (100) surface of synthetic NaCl crystals under conditions of varying humidity, using a concentric electrode configuration and a regular array of square electrodes. Values for the surface resistance were obtained by fitting arcs to data observed in complex impedance plots. Using the Nernst-Einstein equation, these were related to the effective surface diffusivity S, defined as the product of the diffusivity D of NaCl in the water film adsorbed to the crystal surfaces, the surface film thickness δ and the solubility C of NaCl in the surface film. Diffusivity values were estimated assuming a solubility equal to that in bulk solution and values for δ consistent with previous work on water adsorption of NaCl. The following conclusions can be drawn:

[49] 1. Values for S range from 1×10^{-27} m^3 s^{-1} at very dry conditions (1 g/m^3 AH or 4% RH) to 1×10^{-19} m^3 s^{-1} for absolute humidities of 18 g/m^3 (78% RH). The values obtained at high humidities are in reasonable agreement with existing values for the effective diffusivity of NaCl in grain boundary brine films suggesting the system behaves as if saturated brine is present. A change in slope is observed around 8 g/m^3 absolute humidity (35%–40% RH), which can be explained by water adsorption models that describe a change in water structure from two-dimensional networks to three-dimensional hydrogen-bonded layers. In addition, measured anisotropy might be related to diffusion along surface cleavage steps.

[50] 2. Assuming a constant solubility of 0.165 m^3 m^{-3} and a mean adsorbed film thickness of 50–90 nm, our results imply values for the diffusivity in the range from 1×10^{-14} to 8×10^{-12} m^2 s^{-1} for the highest humidities investigated (14–18 g/m^3 AH, 60%–78% RH), i.e., where the structure of the adsorbed film is believed to resemble liquid water. These values are consistent with previous studies of diffusivity in intergranular brine films during pressure solution but are 2 to 5 orders of magnitude lower than bulk solution values. It is important to obtain better estimates for the thickness of the adsorbed fluid film in order to quantify the diffusivity more accurately.

[51] 3. In geological storage systems in rock salt, where humidities are expected to lie between 14 g/m^3 AH (60% RH at room temperature) and the deliquescence point, we predict values for the effective surface diffusivity in the range $1 \times 10^{-22} - 8 \times 10^{-18}$ m^3 s^{-1}. This implies that crack healing rates might be 6 to 7 orders of magnitude slower than expected for brine-filled cracks, and that cracks in dilated salt may take periods of the order of 1000 years to disconnect under storage system conditions. In future modeling studies of surface-energy driven diffusive crack healing in the EDZ surrounding openings or boreholes in salt, the present effective diffusivity values should be taken into account to ensure reliable estimates of the time needed for healing, i.e., for the salt to recover its natural, low permeability.

[52] **Acknowledgments.** Our appreciation goes out to Eimert de Graaf, Peter van Krieken and Gert Kastelein for their help and technical support during this project. We thank the Associate Editor (Yves Bernabe), Reviewer Tohru Watanabe and an anonymous reviewer for detailed comments, which greatly improved the manuscript. We also thank the Nuclear Energy and Research Group (NRG – Jacques Grupa and Arjen Poley) for discussions and for financial support for parts of the work, which was realized via NRG involvement in the THERESA Project (Work Package 3) of the EC Euratom Sixth Framework Program.

References

Alkan, H., Y. Cinar, and G. Pusch (2007), Rock salt dilatancy boundary from combined acoustic emission and triaxial compression tests, *Int. J. Rock Mech. Min. Sci.*, *44*, 108–119, doi:10.1016/j.ijrmms.2006.05.003.

Barraclough, P. B., and P. G. Hall (1974), The adsorption of water vapour by lithium fluoride, sodium fluoride and sodium chloride, *Surf. Sci.*, *46*, 393–417, doi:10.1016/0039-6028(74)90316-1.

Barsoukov, E., and J. R. Macdonald (Eds.) (2005), *Impedance Spectroscopy: Theory, Experiment, and Applications*, 2nd ed., 595 pp., John Wiley, Hoboken, N. J.

Benson, G. C., and K. S. Yun (1967), Surface energy and surface tension of crystalline solids, in *The Solid/Gas Interface*, vol. 1, edited by E. A. Flood, pp. 203–269, Edward Arnold, London.

Brantley, S. L., B. Evans, S. H. Hickman, and D. A. Crerar (1990), Healing of microcracks in quartz: Implications for fluid flow, *Geology*, *18*, 136–139, doi:10.1130/0091-7613(1990)018<0136:HOMIQI>2.3.CO;2.

Chen, D. L., B. Weiss, and R. Stickler (1996), A model for crack closure, *Eng. Fract. Mech.*, *53*, 493–509, doi:10.1016/0013-7944(95)00169-7.

Cinar, Y., G. Pusch, and V. Reitenbach (2006), Petrophysical and capillary properties of compacted salt, *Transp. Porous Media*, *64*, 199–228, doi:10.1007/s11242-005-2848-1.

Cosenza, P., and M. Ghoreychi (1999), Effects of very low permeability on the long-term evolution of a storage cavern in rock salt, *Int. J. Rock Mech. Min. Sci.*, *36*, 527–533, doi:10.1016/S0148-9062(99)00018-2.

Cristescu, N., and U. Hunsche (1998), *Time Effects in Rock Mechanics*, vol. 1, *Mater. Model. Comput.*, 342 pp., John Wiley, Chichester, U. K.

Dai, Q., J. Hu, and M. Salmeron (1997), Adsorption of water on NaCl (100) surfaces: Role of atomic steps, *J. Phys. Chem. B*, *101*, 1994–1998, doi:10.1021/jp9625772.

De Meer, S., C. J. Spiers, C. J. Peach and T. Watanabe (2002), Diffusive properties of fluid-filled grain boundaries measured electrically during active pressure solution, *Earth Planet. Sci. Lett.*, *200*, 147–157, doi:10.1016/S0012-821X(02)00585-X.

De Meer, S., C. J. Spiers, and S. Nakashima (2005), Structure and diffusive properties of fluid-filled grain boundaries: An in-situ study using infrared (micro) spectroscopy, *Earth Planet. Sci. Lett.*, *232*, 403–414, doi:10.1016/j.epsl.2004.12.030.

Enapu, F. O., and A. K. Jonscher (1987), Time- and frequency-dependent surface transport on humid insulators, in *Annual Report: Conference on Electrical Insulation and Dielectric Phenomena, October 18–22, 1987, National Bureau of Standards, Gaithersburg, Maryland*, Inst. of Electr. and Electron. Eng., Washington, D. C.

Ewing, G. E. (2005), H_2O on NaCl: From single molecule, to clusters, to monolayer, to thin film, to deliquescence, *Struct. Bonding*, *116*, 1–25, doi:10.1007/430_012.

Ewing, G. E. (2006), Ambient thin film water on insulator surfaces, *Chem. Rev.*, *106*, 1511–1526, doi:10.1021/cr040369x.

Ewing, R. C. (1999), Less geology in the geological disposal of nuclear waste, *Science*, *286*, 415–417, doi:10.1126/science.286.5439.415.

Fölsch, S., and M. Henzler (1991), Water adsorption on the NaCl surface, *Surf. Sci.*, *247*, 269–273, doi:10.1016/0039-6028(91)90136-G.

Foster, M., and G. E. Ewing (1999), An infrared spectroscopic study of water thin films on NaCl (100), *Surf. Sci.*, *427–428*, 102–106, doi:10.1016/S0039-6028(99)00242-3.

Foster, M., and G. E. Ewing (2000), Adsorption of water on the NaCl(001) surface. II. An infrared study at ambient temperatures, *J. Chem. Phys.*, *112*, 6817, doi:10.1063/1.481256.

Gavrilenko, P., and Y. Gueguen (1989), Pressure dependence of permeability: A model for cracked rocks, *Geophys. J. Int.*, *98*, 159–172, doi:10.1111/j.1365-246X.1989.tb05521.x.

Gel'perin, N. I., B. M. Gurovich, and K. K. Dubinchik (1969), Concentration and temperature dependence of the surface tensions of some inorganic substances, *Zh. Prikl. Khim.*, *42*, 214–216.

Heidug, W. K. (1991), A thermodynamic analysis of the conditions of equilibrium at non-hydrostatically stressed and curved solid–fluid interfaces, *J. Geophys. Res.*, *96*, 21,909–21,921, doi:10.1029/91JB02173.

Hickman, S. H., and B. Evans (1987), Influence of geometry upon crack healing rate in calcite, *Phys. Chem. Miner.*, *15*, 91–102, doi:10.1007/BF00307614.

Hickman, S. H., and B. Evans (1992), Growth of grain contacts in halite by solution-transfer: Implications for diagenesis, lithification, and strength recovery, *Int. Geophys.*, *51*, 253–280, doi:10.1016/S0074-6142(08)62825-9.

Hickman, S. H., and B. Evans (1995), Kinetics of pressure solution at halite-silica interfaces and intergranular clay films, *J. Geophys. Res.*, *100*, 13,113–13,132, doi:10.1029/95JB00911.

Hou, M. Z., H. Xie, and J. Yoon (Eds.) (2010), *Underground Storage of CO_2 and Energy*, 384 pp., Balkema, Leiden, Netherlands.

Hucher, M., A. Oberlin, and R. Hocart (1967), Adsorption de vapeur d'eau sur les faces de clivage de quelques halogénures alcalins, *Bull. Soc. Fr. Mineral. Cristallogr.*, *90*, 320–332.

Hunsche, U., and A. Hampel (1999), Rock salt—The mechanical properties of the host rock material for a radioactive waste repository, *Eng. Geol. Amsterdam*, *52*, 271–291, doi:10.1016/S0013-7952(99)00011-3.

Israelachvili, J. N. (1992), *Intermolecular and Surface Forces*, 2nd ed., Academic, San Diego, Calif.

Jonscher, A. K. (1991), Low-frequency dispersion in volume and interface situations, *J. Mater. Sci.*, *26*, 1618–1626, doi:10.1007/BF00544672.

Kim, J. H., and S. B. Lee (2001), Behavior of plasticity-induced crack closure and roughness-induced crack closure in aluminum alloy, *Int. J. Fatigue*, *23*, suppl. 1, 247–251, doi:10.1016/S0142-1123(01)00155-4.

Langer, M. (1993), Use of solution-mined caverns in salt for oil and gas storage and toxic waste disposal in Germany, *Eng. Geol. Amsterdam*, *35*, 183–190, doi:10.1016/0013-7952(93)90005-W.

Langer, M. (1999), Principles of geomechanical safety assessment for radioactive waste disposal in salt structures, *Eng. Geol. Amsterdam*, *52*, 257–269, doi:10.1016/S0013-7952(99)00010-1.

Liang, W., C. Yang, Y. Zhao, M. B. Dusseault, and J. Liu (2007), Experimental investigation of mechanical properties of bedded salt rock, *Int. J. Rock Mech. Min. Sci.*, *44*, 400–411, doi:10.1016/j.ijrmms.2006.09.007.

Lide, D. R. (Ed.) (2000), *CRC Handbook of Chemistry and Physics*, 81st ed., 2556 pp., CRC Press, Boca Raton, Fla.

Liedtke, L., and W. Bleich (1985), Convergence calculations for back-filled tunnels in rock salt, *Comput. Struc.*, *21*, 353–378, doi:10.1016/0045-7949(85)90255-X.

Lindberg, V. (2000), *Uncertainties and Error Propagation: Part I of a Manual on Uncertainties, Graphing and the Vernier Caliper*, Rochester Inst. of Technol., Rochester, N. Y. [Available at http://www.rit.edu/cos/uphysics/uncertainties/Uncertaintiespart1.html.]

Luna, M., F. Rieutord, N. A. Melman, Q. Dai, and M. Salmeron (1998), Adsorption of water on alkali halide surfaces studied by scanning polarization force microscopy, *J. Phys. Chem.*, *102*, 6793–6800, doi:10.1021/jp9820875.

MacDonald, J. R., and W. R. Kenan (1995), *Impedance Spectroscopy: Emphasizing Solid Materials and Systems*, 368 pp., Wiley-Interscience, Hoboken, N. J.

Maryniak, W. A., T. Uehara, and M. A. Noras (2003), Surface resistivity and surface resistance measurements using a concentric ring probe technique, *Tech. Note 1005*, pp. 1–4, Trek, Inc., Medina, N. Y.

Nakashima, S. (1995), Diffusivity of ions in pore water as a quantitative basis for rock deformation rate estimates, *Tectonophysics*, *245*, 185–203, doi:10.1016/0040-1951(94)00234-Z.

Orazem, M. E., and B. Tribollet (2008), *Electrochemical Impedance Spectroscopy*, 560 pp., Wiley-Interscience, Hoboken, N. J.

Ozdemir, O., S. I. Karakashev, A. V. Nguyen, and J. D. Miller (2009), Adsorption and surface tension analysis of concentrated alkali halide brine solutions, *Miner. Eng.*, *22*, 263–271, doi:10.1016/j.mineng.2008.08.001.

Paquette, L. A. (1995), *Encyclopedia of Reagents for Organic Synthesis*, 6234 pp., Wiley, Chinchester, U. K.

Paraschiv-Munteanu, I., and N. D. Cristescu (2001), Stress relaxation during creep of rocks around deep boreholes, *Int. J. Eng. Sci.*, *39*, 737–754, doi:10.1016/S0020-7225(00)00060-4.

Peach, C. J., and C. J. Spiers (1996), Influence of crystal plastic deformation on dilatancy and permeability development in synthetic salt rock, *Tectonophysics*, *256*, 101–128, doi:10.1016/0040-1951(95)00170-0.

Peach, C. J., C. J. Spiers, and P. W. Trimby (2001), Effect of confining pressure on dilatation, recrystallization, and flow of rock salt at 150°C, *J. Geophys. Res.*, *106*, 13,315–13,328, doi:10.1029/2000JB900300.

Peters, S. J., and G. E. Ewing (1997a), Water on salt: An infrared study of adsorbed H_2O on NaCl(100) under ambient conditions, *J. Phys. Chem.*, *101*, 10,880–10,886, doi:10.1021/jp972810b.

Peters, S. J., and G. E. Ewing (1997b), Thin film water on NaCl(100) under ambient conditions: An infrared study, *Langmuir*, *13*, 6345–6348, doi:10.1021/la970629o.

Roberts, J. J., and J. A. Tyburczy (1993), Impedance spectroscopy of single and polycrystalline olivine: Evidence for grain boundary transport, *Phys. Chem. Miner.*, *20*, 19–26, doi:10.1007/BF00202246.

Rutter, E. H. (1983), Pressure solution in nature, theory and experiment, *J. Geol. Soc.*, *140*, 725–740, doi:10.1144/gsjgs.140.5.0725.

Senseny, P. E., F. D. Hansen, J. E. Russell, N. L. Carter, and J. W. Handin (1992), Mechanical behaviour of rock salt: Phenomenology and micromechanisms, *Int. J. Rock Mech. Min. Sci. Geomech. Abstr.*, *29*, 363–378, doi:10.1016/0148-9062(92)90513-Y.

Shinto, H., T. Sakakibara, and K. Higashitani (1998), Molecular dynamics simulations of water at NaCl(001) and NaCl(011) surfaces, *J. Phys. Chem.*, *102*, 1974–1981, doi:10.1021/jp972795a.

Silberschmidt, V. G., and V. V. Silberschmidt (2000), Analysis of cracking in rock salt, *Rock Mech. Rock Eng.*, *33*, 53–70, doi:10.1007/s006030050004.

Simkovich, G. (1963), The surface conductance of sodium chloride crystals as a function of water vapor partial pressure, *J. Phys. Chem.*, *67*, 1001–1004, doi:10.1021/j100799a013.

Smith, D. L., and B. Evans (1984), Diffusional crack healing in quartz, *J. Geophys. Res.*, *89*, 4125–4135, doi:10.1029/JB089iB06p04125.

Spiers, C. J., and P. M. T. M. Schutjens (1999), Intergranular pressure solution in NaCl: Grain-to-grain contact experiments under the optical microscope, *Oil Gas Sci. Technol.*, *54*, 729–750, doi:10.2516/ogst:1999062.

Spiers, C. J., P. M. T. M. Schutjens, R. H. Brzesowsky, C. J. Peach, J. L. Liezenberg, and H. J. Zwart (1990), Experimental determination of constitutive parameters governing creep of rock salt by pressure solution, in *Deformation Mechanism, Rheology and Tectonics*, edited by R. J. Knipe and E. H. Rutter, pp. 215–227, Geol. Soc., London.

Ten Grotenhuis, S. M., M. R. Drury, C. J. Peach, and C. J. Spiers (2004), Electrical properties of fine-grained olivine: Evidence for grain boundary transport, *J. Geophys. Res.*, *109*, B06203, doi:10.1029/2003JB002799.

Ter Heege, J. H., J. H. P. De Bresser, and C. J. Spiers (2004), Dynamic recrystallization of dense polycrystalline NaCl: Dependence of grain size distribution on stress and temperature, *Mater. Sci. Forum*, *467–470*, 1187–1192, doi:10.4028/www.scientific.net/MSF.467-470.1187.

Ter Heege, J. H., J. H. P. De Bresser, and C. J. Spiers (2005), Rheological behaviour of synthetic rocksalt: The interplay between water, dynamic recrystallization and deformation mechanisms, *J. Struct. Geol.*, *27*, 948–963, doi:10.1016/j.jsg.2005.04.008.

Watanabe, T., and C. J. Peach (2002), Electrical impedance measurement of plastically deforming halite rocks at 125°C and 50 MPa, *J. Geophys. Res.*, *107*(B1), 2004, doi:10.1029/2001JB000204.

P. J. Koelemeijer, Bullard Laboratories, Department of Earth Sciences, University of Cambridge, Madingley Rise House, Madingley Road, Cambridge CB3 0EZ, UK. (pjk49@cam.ac.uk)

C. J. Peach and C. J. Spiers, High Pressure and Temperature Laboratory, Faculty of Geosciences, Utrecht University, PO Box 80.021, NL-3508 TA Utrecht, Netherlands.